

## EFFECT OF MICROSTRUCTURE AND RELATIVE HUMIDITY ON ATMOSPHERIC PITTING CORROSION OF DUPLEX STAINLESS STEEL BENEATH $MgCl_2$ DROPS

Safa Abdulkhaliq Ali <sup>a\*</sup>, Haval Bashar Mohammed-Ali <sup>b</sup><sup>a</sup> Department of Physics, Faculty of Science, University of Zakho, Zakho, Kurdistan Region-Iraq. ([safa.ali@staff.uoz.edu.krd](mailto:safa.ali@staff.uoz.edu.krd))<sup>b</sup> Department of Physics, Faculty of Science, University of Zakho, Zakho, Kurdistan Region-Iraq. ([haval.balatay@uoz.edu.krd](mailto:haval.balatay@uoz.edu.krd))

Received: 30 Oct., 2022 / Accepted: 19 Dec., 2022 / Published: 30 May, 2023

<https://doi.org/10.25271/sjuoz.2023.11.2.1047>

### ABSTRACT

One of the main issues for intermediate-level nuclear waste (ILW) is atmospheric corrosion in stainless steel. The impact of microstructure on the pit shapes on three orientations of the duplex stainless steel DSS 2205 plate and the relative humidity impact on the atmospheric corrosion pits of DSS beneath  $MgCl_2$  drops is determined through the use of four characterization tools: X-ray diffraction (XRD), Energy dispersive X-ray (EDX) analyses, Scanning electron microscopy (SEM), and optical microscopy. The pits on the top surface (LT) appears layered like an attack and mostly hemispherical, while the long transverse (LS) and short transverse (ST) planes reveal elongated strings. The map scan of EDX indicates mixed oxide inclusions and MnS inclusion existing in the steel alloy and the XRD analyses present the existence of two-phase both austenite  $\gamma$  and ferrite  $\alpha$  peaks. The pit shape and area were influenced by relative humidity (RH) change. At RH 35% the trend of pits in 1-week exposure revealed a larger area of pit mouth than in RH 45%. For the same exposure time and in both RHs, the area seemed to be greater at the droplet's center than in the edge of the droplet.

**Keywords:** Atmospheric Pitting Corrosion, Duplex Stainless Steel, Microstructure, Relative Humidity,  $MgCl_2$  Drops

### 1. INTRODUCTION

DSSs are a unique category of steel that includes ( $\geq 11\%$  Cr by weight) with a balanced ratio of two phases austenite ( $\gamma$ ) and ferrite ( $\alpha$ ) (Örnek, 2015; Rodrigues *et al.*, 2019). They are frequently employed in power industries, offshore, and chemical conditions and presently the plan is to make them the compensated container for (intermediate level nuclear radioactive waste) ILW as it is a vast worry in the UK's nuclear industry, because of their remarkable corrosion resistance and mechanical qualities in comparison to austenite grades (Potgieter *et al.*, 2008; Örnek, 2015; Örnek and Engelberg, 2015). The benefits of ferrite with austenite phases are combined in duplex alloys (Potgieter *et al.*, 1996; Mampuya *et al.*, 2021), which offer various features, notably resistance to corrosion within a corrosion environment containing Cl<sup>-</sup> ions, ductility, mechanical strength, and weldability (Cvijović and Radenković, 2006; Tan *et al.*, 2011; Pramanik, Bera and Ghosh, 2014). Nevertheless, it is not avoidable to pitting corrosion as its other counterparts such as (austenite stainless steel) ASS (Ghahari *et al.*, 2015), which occurs when the passive layer breaks locally beneath specific structural and ambient circumstances such as a Cl<sup>-</sup> rich environment.

It is normally agreed that microstructure can impact pit onset (Lo and Tsai, 2007; Deng *et al.*, 2009), with focus on sulfide inclusion in particular (Stewart and Williams, 1992) and the majority of earlier investigations have concentrated on MnS inclusions as they have been recognized to be a more efficient initiator of pits corrosion (Wranglen, 1974; Mohammad-Ali, 2016; Park and Kang, 2017). It has been clear that elongated inclusions play a vital role in pit initiating and growing in SSs (Mohammad-Ali, 2016), a study confirmed by Mair and Frankel *et al.* (Maier and Frankel, 2010). Moreover, ferrite orientation severely impacts the atmospheric pit shapes, Pitting traced the ferrite bands on the (LS) and (ST) planes of 304L SS and extended into the pit through corrosion as confirmed by Mohammad-Ali *et al.* (2018) It is mostly believed that in duplex stainless steel the majority presented inclusions are mixed oxides inclusions (Zhang *et al.*, 2020; Lei *et al.*, 2021), Yauhua Zhang

(Zhang *et al.*, 2020) examined the oxide-inclusions presented in 2205 DSS, and results illustrate that three types of oxide-inclusions exist in the steel one of them named Al-Mg-O type of inclusion.

Another key parameter that enhances the probability of atmospheric corrosion of pits is the relative humidity. RH is crucial since the solution droplets concentration and/or electrolyte layer is defined by (RH). The Cl<sup>-</sup> content within the solution droplet rises as the humidity declines, improving the chances of corrosion of pits (Tsutsumi, Nishikata and Tsuru, 2007). The importance of initial droplet concentration which is CDD cannot be unnoticed because it is one of the factors that determine the pit location as investigated by Street *et al.* (Street *et al.*, 2015, 2018).  $MgCl_2$  is broadly utilized for atmospheric corrosion testing of stainless steel (Tsutsumi, Nishikata and Tsuru, 2007; Maier and Frankel, 2010). Since it is a prevalent component in seawater with a small deliquescence point 35%, rendering it is more prone than NaCl 75% to produce pitting. The impact of RH on atmospheric corrosion pits of ASS 304L has been reported by numerous studies (Van Nam, Tada and Nishikata, 2015; Laya-Guo, 2019; Weirich *et al.*, 2019). Guo *et al.* (Laya-Guo, 2019) elucidated that varying RH values (between 33%, 85%, and 12%) cause the formation of numerous pits, whilst continual exposure at a constant 33% RH gives rise to single pit growth. Also Tsutsumi *et al.* (Tsutsumi, Nishikata and Tsuru, 2005, 2007) studied the impacts of RH on the Cl<sup>-</sup> ion concentration of  $MgCl_2$  placed on 304 austenite stainless steel at room temperature and observed that the critical atmospheric-induced Cl<sup>-</sup> concentration upon which stable corrosion of pits takes place at 298K is roughly 6M, relating to 65% RH. A work conducted on austenite stainless steel 304L and 316L that pit morphology is influenced by the value of RH, at smaller RH values satellite and earing pits are obtained whereas at upper RH only pits of circle shape are determined (Mohammad-Ali, 2016).

More recent works have been reported regarding the atmospheric corrosion and the microstructure of stainless steel (Zhu *et al.*, 2020; Wang and Wang, 2021; Devaraj, 2022; Li *et al.*, 2022; Sheik *et al.*, 2022; Yoon and Ahn, 2022; Moreira *et al.*, 2023)

\* Corresponding author

This is an open access under a CC BY-NC-SA 4.0 license (<https://creativecommons.org/licenses/by-nc-sa/4.0/>)

The novelty of this work lies in its focus on the role of relative humidity variation with the microstructure on atmospheric pitting corrosion of duplex stainless steel plate grade 2205 under droplets of MgCl<sub>2</sub>.

**2. EXPERIMENTAL PROCEDURES**

**2.1 Material and sample preparation**

The employed alloy in this work was a cooled rolled DSS plate of grade 2205 which is called an as-received sample with composition (by weight%) presented in Table 1. Figure.1 is an illustration of the three orientations top surface plane (LT), side grain (LS) plane, and end grain (ST) plane which were cut by cutting wheels into dimensions of 20×20 mm for LT, and 2×20 mm for LS and ST respectively along the rolling direction (RD) with 2 mm thickness.

Table 1 The Chemical compositions of DSS alloy used in this work.

Elements	C	Si	Mn	P	S	Cr	Ni	Mo	Nb	Cu	Co	N	Fe
wt. %	0.15	0.4	1.4	0.22	0.001	22.42	5.73	3.15	0.13	0.26	0.13	0.168	Balance

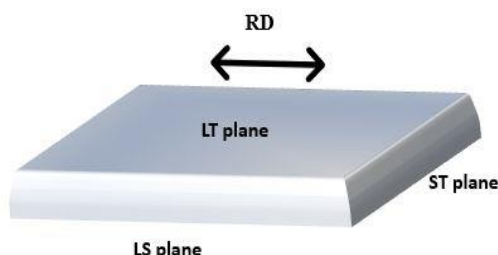


Figure 1 Plate planes and the rolling direction.

**2.2 Lab-based corrosion tests:**

The specimens were cold mounted and oriented to subject the top surface plane (LT), surfaces, side grain (LS) plane, and end grain (ST) plane for analyzing the impact of relative humidity variation. All tests were achieved firstly by grinding 2205 specimen with 800-grit SiC paper, splashed with deionized water

(DI), and then ultrasonically cleaned with DI water for 5 minutes followed by drying the specimens' surface via cold air. The specimens were then sealed in a desiccator within the surrounding condition for 24 hours. Tests were done by placing the droplets of MgCl<sub>2</sub> solution on the DSS specimens for one 1 week. A summary of test details is outlined in Table 2.

Table 2 Summarized results of corrosion tests and the pits likelihood take place on three plate- orientations of DSS 2205 under 0.4M droplets of MgCl<sub>2</sub> with 1.1µl which were kept at 30 °C±2 with CDD~650 µg/cm<sup>2</sup>.

Exposure time	RH %	Orientation	Material condition	Number of pits
1 week	35%	LT	As received	16/16
		LS	As received	5/10
		ST	As received	10/10
	45%	LT	As received	4/20
		LS	As received	×
		ST	As received	1/9
	56%	LT	As received	×
		LS	As received	×
		ST	As received	×

**2.3 Droplet deposition**

The salt solution was prepared from (MgCl<sub>2</sub>.6H<sub>2</sub>O) (HIMEDIA) with DI water. A micropipette of 0.5-2.5 µl volume and 0.81% inaccuracy was used for droplet deposition. 1.1 µl droplets of 0.4M MgCl<sub>2</sub> were placed on the specimen, FigureFigure 2

demonstrates the deposition of MgCl<sub>2</sub> droplets on the top surface of the DSS specimen. It took about 3-4 minutes to deposit 16 droplets. The area of the droplet was 0.54 mm<sup>2</sup> using FIGI/IMAGE J software, giving a chloride deposition density (CDD) value~650 µg/cm<sup>2</sup>.

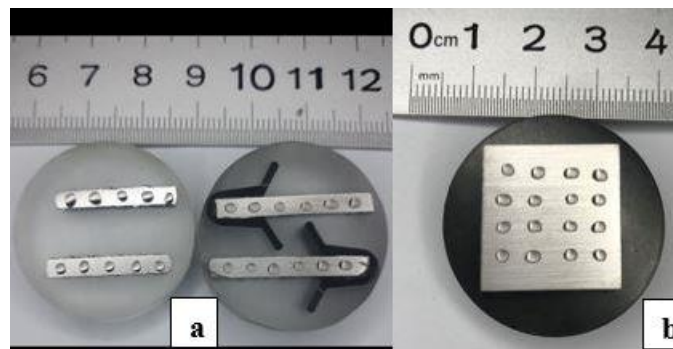


Figure 2 Droplet deposition on DSS samples by using micropipette a-LS and ST plate planes b-LT plate plane.

#### 2.4 Saturated salt for RH and temperature control

Saturated salt solutions that were employed to retain the RH of atmospheric corrosion tests are  $\text{MgCl}_2 \cdot 6\text{H}_2\text{O}$  (35% RH),  $\text{K}_2\text{CO}_3$  (45% RH), and  $\text{NaBr}$  (56% RH) (ASTM, 1985). The effective temperature range of  $\text{MgCl}_2 \cdot 6\text{H}_2\text{O}$  and (56% RH) is 5-80 °C while that for  $\text{K}_2\text{CO}_3$  is 5-30 °C (ASTM, 1985). Solutions were kept in covered desiccators for all tests and the temp/humidity were watched with 3 data loggers (1-EL-USB-2-LCD, (2and3-EL-21CFR lascar electronics), then the desiccators were put inside the (NLF64-320) chamber which controlled the temperature at  $(30 \pm 1)^\circ\text{C}$ .

#### 2.5 Microstructural examination

Specimens of duplex SS 2205 grade were cut by cutting wheels into 20×20 mm for (LT) top surface plane, 20×5 mm surfaces of side grain (LS) plane, and end grain (ST) plane. They were mounted in a Bakelite, and employed for the effect of microstructure, then ground with 800grit SiC paper and polished with 6, 3, 1 micron of (Water-based monocrystalline diamond suspension) then etched with Kalling's 2 reagent (5g  $\text{CuCl}_2$ , 100 ml HCl, and 100 ml ethanol) up to 5 seconds at lab temperature roughly (20°C). The base alloy's microstructure was investigated by scanning electron microscopy (SEM) Quanta 450 equipped with the detector of energy dispersive X-ray spectroscopy (EDX) for analyzing the chemical composition. X-ray diffraction analysis PAN analytical X' Pert PRO ( $\text{Cu K}\alpha=1.5406 \text{ \AA}$ ) were performed to evaluate the presence of ( $\gamma/\alpha$ ) phases.

#### 2.6 Measurement of pit mouth area

A Leica DM4500P polarized optical microscope was used for photographing each pit. The area of the pit was measured in similar means as droplet area measurements by using the wand tool in FIJI/ImageJ software, by which the pit's edge was clicked to trace a uniform. This was followed by choosing legacy mode

plus tolerance value which was set on ten, then the measurement tool was clicked and the area was obtained. The area values then were converted to diameters to facilitate the calculations using the equation  $A = \pi r^2$ , considering that the pit area was circular

#### 2.7 Measurements of pit depth

A Leica DM4500P polarized optical microscope was used for measuring the depth of each pit found in lab experiments. The variation between the optical focus on the sample's surface with the optical focus on the pit's base was used to determine the depth of the pit (the lowest viewed point).

### 3 RESULTS AND DISCUSSION

#### 3.1 Microstructure

The XRD patterns for the as-received LT specimen of DSS 2205 are shown in Figure 3. There are six peaks consisting of two basic phases  $\gamma$  austenite and  $\alpha$  ferrite phases respectively without any other precipitation or phases. However, it was studied in earlier works on DSS that the (deformation induced martensite DIM)  $\alpha'$  might form at peak ( $2\theta=72.20$ ) throughout the cold working process that shares the identical crystallographic characteristics of the ferrite phase (Pramanik, Bera and Ghosh, 2014; Rodrigues *et al.*, 2019).

The SEM scanning of the microstructure (0 - 10  $\mu\text{m}$ ) of three plate orientations of the specimen after final polishing followed by etching in Kalling's 2 reagent is revealed in Figure 4. It is readily apparent the duplex steels are rolled into a fine elongated structure of austenite and ferrite lamellar, where the light gray region is austenite ( $\gamma$ ) phase and the dark gray region is ferrite ( $\alpha$ ). It is also indicated from the SEM image that only the austenite phase and ferrite phase have seemed in the base metal as confirmed by (Örnek, 2015). The grains of austenite in both rolling directions and longitudinal are continuous, however, wider on the rolling and appear thinner on the longitudinal, perhaps the reason is the pressing deformation of the rolling process of manufacturing (Mampuya *et al.*, 2021).

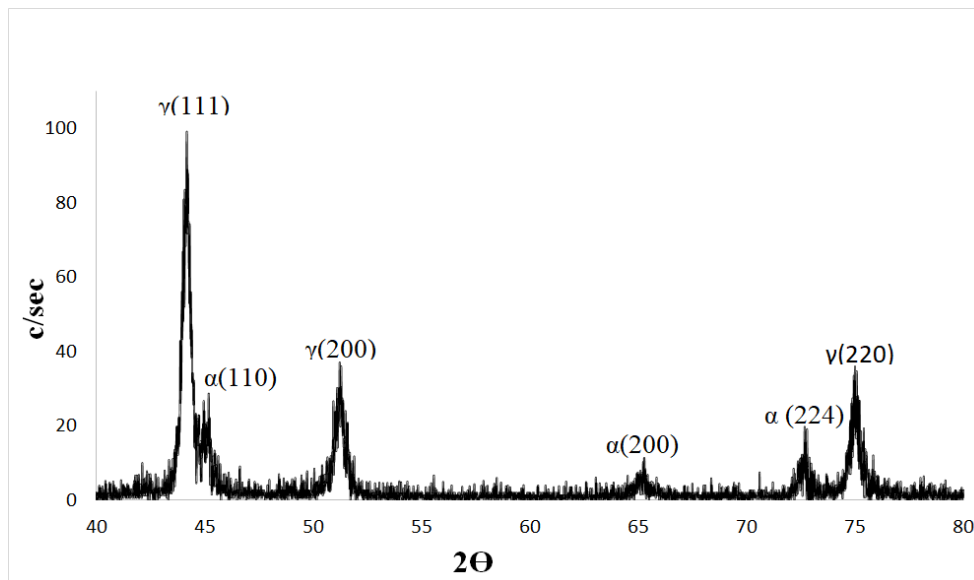


Figure 3 XRD pattern of the top surface LT of DSS 2205.

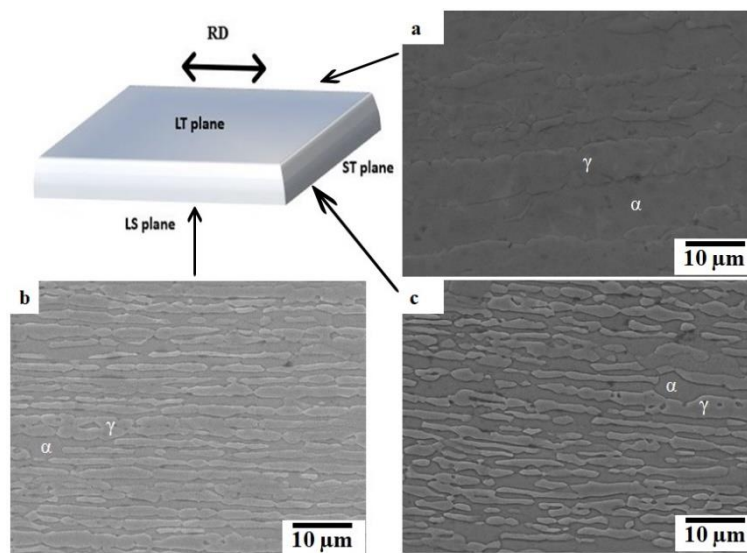


Figure 4 Microstructure of three plate orientations of grade 2205 duplex stainless steel for as-received condition.

### 3.2 Characterization of inclusions in DSS

Inclusion characterization on the LS side for the studied alloy was achieved by SEM and EDX in turn. Mixed oxide inclusions with MnS inclusions on the LS plane of base 2205 duplex stainless steel are revealed in Figures 5-a and b. The EDX analyses for mixed oxides inclusions were completed to detect their chemical compositions.

The image of SEM illustrates that those inclusions existing in this type of steel have many forms for example circular and elliptical and elongated-like shape inclusions as seen in Figure 5-a. As appears in Figure 6 the prevalent type of inclusions are mixed oxide inclusions of Al-Mg-O type consistent with their composition this is reliable with the results conducted by the Yauhua Zhang group (Zhang *et al.*, 2020) who found that three types of oxide inclusions are contained in the steel 2205 such as Al-Mg-O based upon their elemental composition.

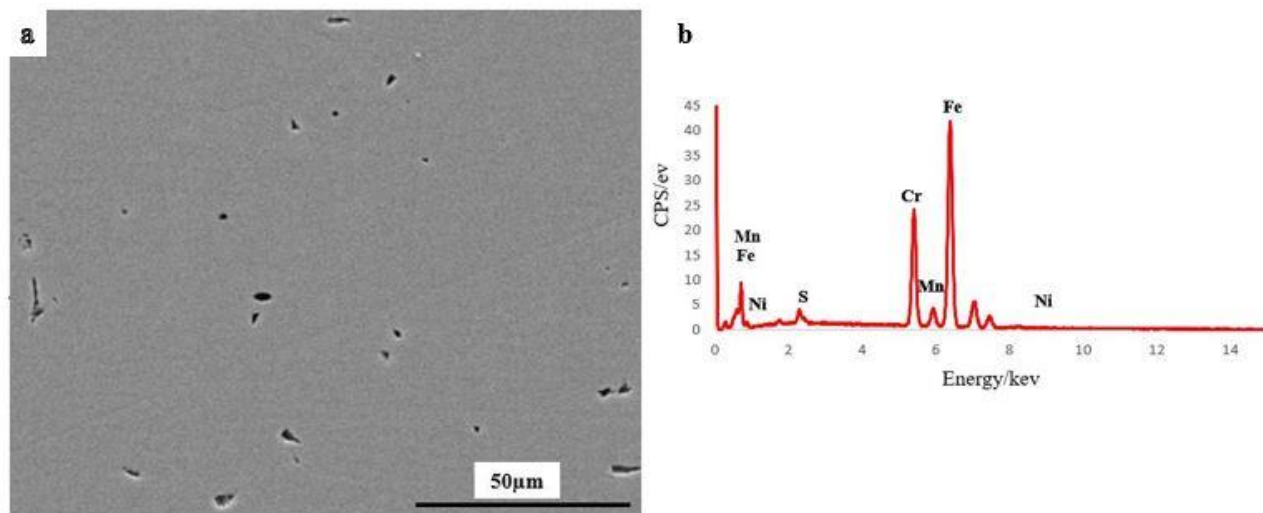


Figure 5-a SEM view of mixed oxide inclusions on LS plane of DSS 2205 after final polishing b-EDX scan for a typical example of MnS inclusion.

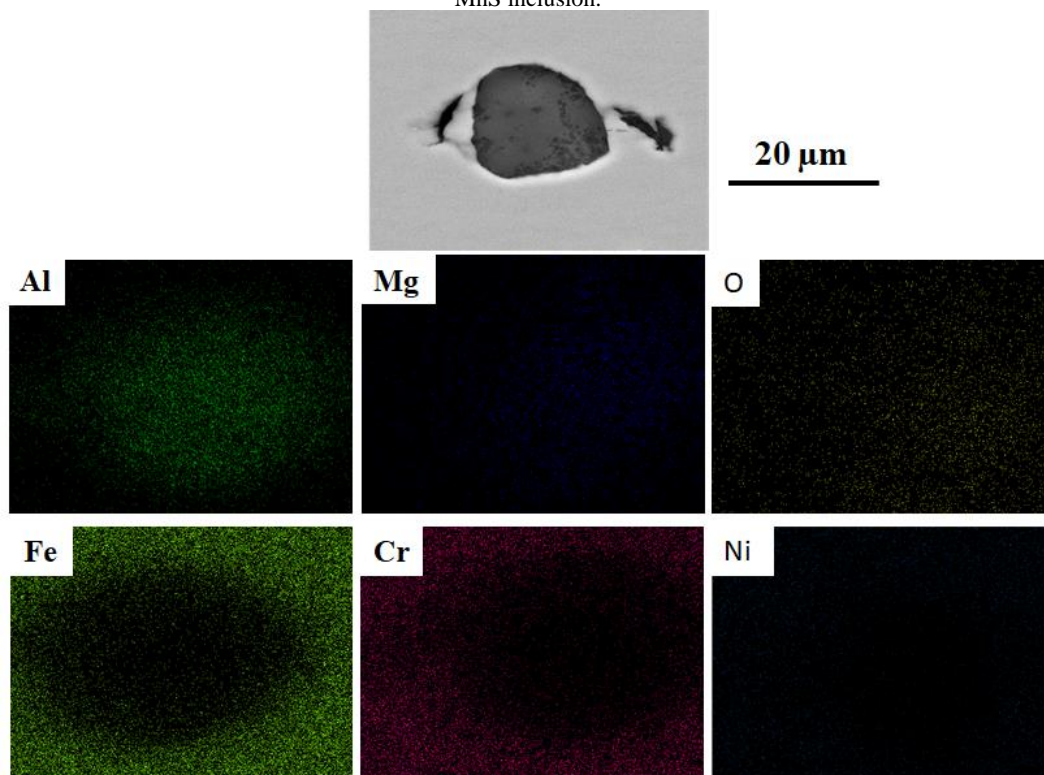


Figure 6 A magnified SEM image of mixed oxide inclusion observed on LS side of final polished base 2205 DSS with EDX analyses of the elemental map.

### 3.3 Effect of plate orientation on the morphology of pits

For the DSS alloy, the impact of three orientations of the plate on the morphology of pits was examined. Specimens were

examined for the period of 1-week for three various RH 35%, 45%, and 56%. Corrosion of pits was observed in both RH 35% and 45% conditions.

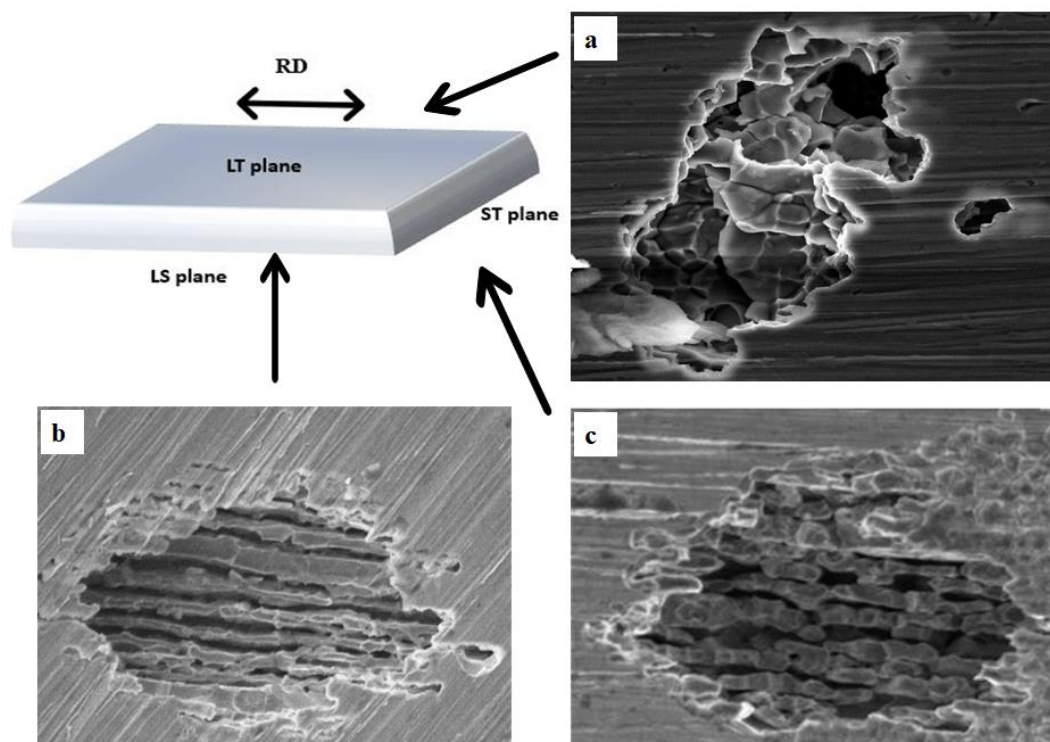


Figure 7 SEM analysis of pits formed on three DSS plate orientations beneath  $\text{MgCl}_2$  droplets with CDD value  $\sim 650 \mu\text{g}/\text{cm}^2$ , at  $30^\circ\text{C}$ , after an exposure time of 1 week at 35% RH.

Figure 7 highlights the morphology of pits formed on the DSS plate orientations LT, LS, and ST planes. The LT plate illustrates a layered attack shape that appears to grow down into the metal, whereas, both LS and ST planes demonstrate the striped morphology of long undissolved metal strands corresponding to the rolling direction. There is a correlation between the microstructure and the morphology of pits observed (see Figure 4 and 7). These results are consistent with the work done by Mohamed-Ali et al (Mohammad-Ali, 2018) who investigated the effect of microstructure of 304L plate of austenite stainless steel on atmospheric pits corrosion beneath  $\text{MgCl}_2$  droplets. Their results of 1-week exposure at 35% RH condition and  $30^\circ\text{C}$  obtained that the austenite ss LT plate showed ring-like pits, while the sides of the plate presented a lined morphology. It is frequently detected that preferential attack occurs for DSS either in austenite or ferrite when the atmospheric environment is

mentioned such as chloride deposit. This is determined depending on the exposure circumstances and the nature of the material, selective damage of ferrite bands was produced on atmospheric corrosion pits of ASS a work done by Mohammed-Ali et al (Mohammad-Ali, 2018). Similar results were found, however, beneath full immersion, a work done by Deng et al (Lo and Tsai, 2007) the SEM image of the top surface of DSS 2205 specimen observed that the ferrite phase is preferentially dissolved and resulted in the initiation of cracks.

### 3.4 Effect of pit position on the pit diameter and depth at RH 35%

Inside a droplet, it is common that pits seemed to begin at random and showed no obvious preference for the edge of the droplet or the center of the droplet [22], [23], (Mohammad-Ali, 2016).

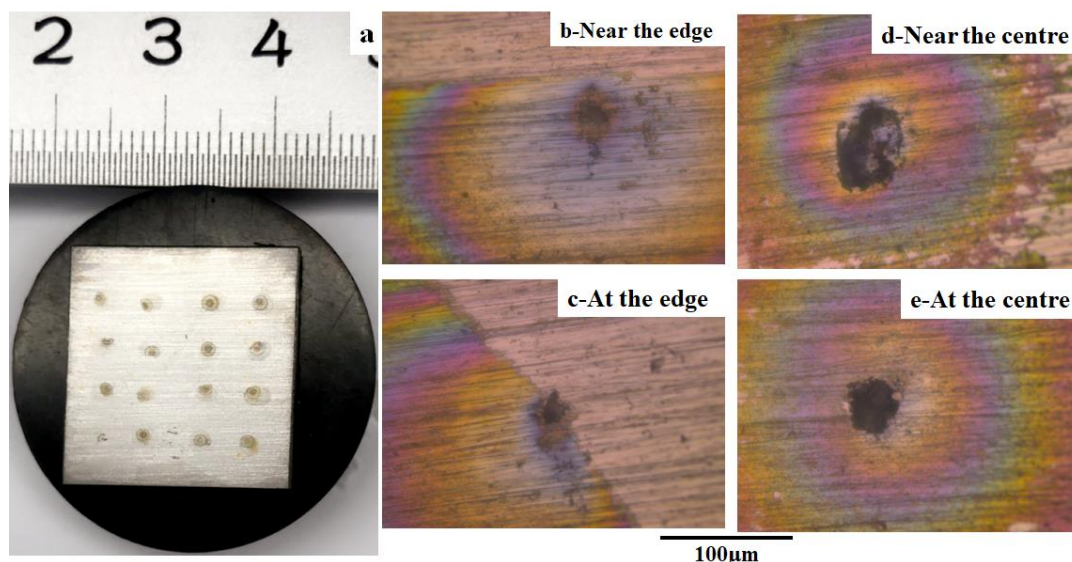


Figure 8 a-A macro image of DSS LT (surface) plate with droplets of MgCl<sub>2</sub> after 1-week exposure at different sample positions: b) near the edge, c) at the edge, d) near the center, and e) at the center.

Figure 8 demonstrates the duplex stainless-steel specimen after washing with pits of RH 35% appears after 1-week of exposure beneath MgCl<sub>2</sub> droplets with ~650 µg/cm<sup>2</sup> chloride deposition density. All 16 droplets pitted, they almost initiate randomly in the droplet containing merely one pit in each droplet. In this RH, however, no complex pit shapes were seen such as satellite and earing. As can be seen in Figure 8, most of the pits were shown to be hemispherical-like in shape. Using an optical microscope, 7 pits were observed at the droplet center, 2 pits at the droplet edge, 4 near the droplet edge, and 2 pits adjacent to the droplet center, only one pit was elongated to the rolling direction this is owing to the microstructure properties. There might be an elongated inclusion in the steel alloy shown in Figure 9. This case has been realized in the work of Mohammed-Ali (Mohammad-Ali, 2016), at RH 45%. It is frequently common that at lower relative humidity the diameter of the pit at or close to the droplet's center is relatively greater than those forms at or close to the edge (Mohammad-Ali, 2016) the reason is probably the rise in IR drop and the solution droplet may be is diluter at the periphery, however, in this study, this is not confirmed. The trend

of pits of 1-week exposure illustrates a comparison of pit mouth diameter of the three various RH shown in Figure 10, it is obvious that the average diameter of pit for RH 35% has the largest area having 82 µm±30 µm which is according to common literature that as the RH increases the diameter of the pit mouth decreases (Mohammad-Ali, 2016; Street *et al.*, 2018). The rise in pit diameter can be correlated to a work done by Ghahari *et al.* (Ghahari *et al.*, 2015) who observed the growth in the surface area of a pit as the current fluctuates leading to a pit of a lacy shape.

Under RH of 35%, the average depth of pits was 26±9 µm after one-day exposure and it was increased to 40±7 µm after a one-week duration as shown in Figure 11. The results observed in this research are in agreement with the work done by Mohammed-Ali (Mohammad-Ali, 2016) and Majid Ghahari *et al.* [10]. The later research showed that the exposure time and pit depth are linearly dependent. It is worth mentioning that the pits can propagate horizontally (undercutting following the microstructure orientations) and cannot be observed from top view using the optical microscope.

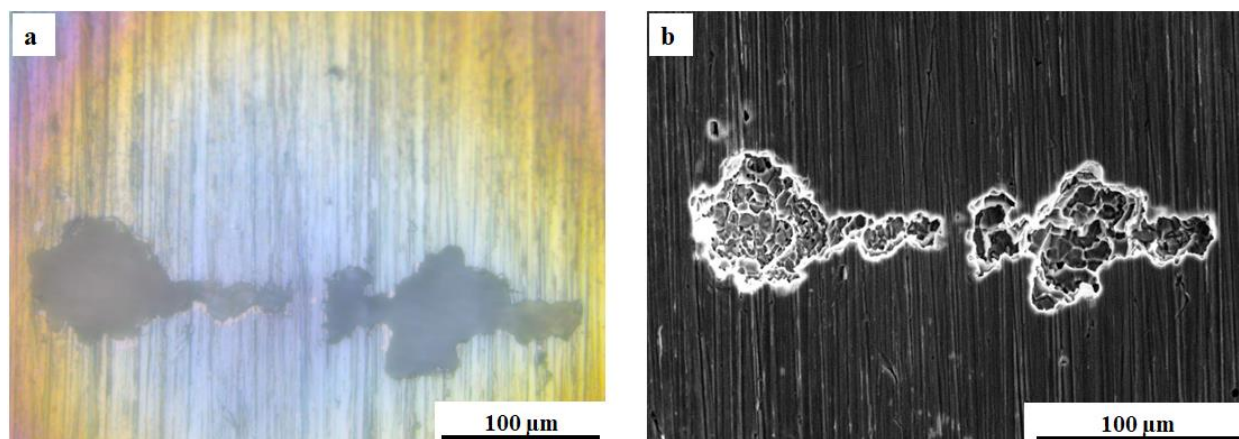


Figure 9 a) optical microscope, and b) SEM images of an elongated pit along the rolling direction formed on the LT side of DSS.

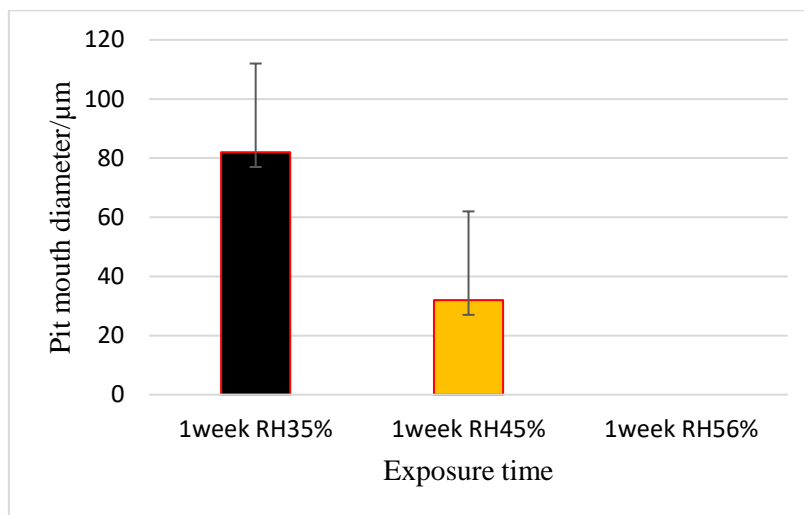


Figure 10 Pit mouth diameter variation against exposure time under different RH.

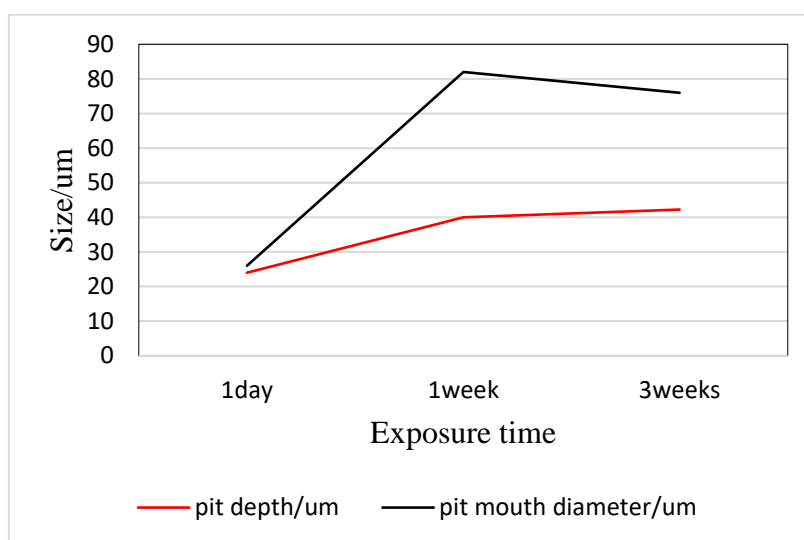


Figure 11 Variation of pit size as a function of exposure time under RH 35% at 30 °C.

**3.5 Effect of pit position on the pit diameter and depth at RH 45%**

Similar to RH 35%, the RH 45% also showed the layer attacked shape under the same conditions. Both LS and ST planes demonstrate the striped morphology of long undissolved metal strands parallel to the rolling direction. It should be noted that out of 20 droplets only 4 droplets were pitted. 2 pits were formed adjacent to the center of the droplet, 1 at the edge, and the last one was bisected at the edge.

Under RH 45%, no complex pit morphology was seen. Moreover, both pits near the droplet center showed larger pits diameter having (30 μm) compared to the pit observed at the edge of the

droplet (25 μm). Based on the observations, the pits mouth and pits depth values of RH 45% were lower than those of RH 35% as shown in Table 3. This was achieved in the work of Mohammed-Ali (Mohammad-Ali, 2016) and Street (Street et al., 2015, 2018). Street found that in the RH 35%, 45%, and 48% situation, droplets tended to have a greater diameter in the center, whereas pits that formed towards the droplet edge were smaller and showed less diameter change than pits that developed at the droplet center. The reason is probably the rise in IR decline that causes the diameter of the dish region to become smaller. For the period of the 1-week pit, depth was 28±5 μm, however, compared to the values at RH 35% for the same trend they were smaller, as highlighted in Table 3.

Table 3 Pit diameter and depth as a function of relative humidity Pits formed on 304L stainless steel (top surface (LT)) under MgCl<sub>2</sub> droplets (~2.5 mm average diameter, CDD ~650 μg/cm<sup>2</sup> CDD for 1 week at 30 °C.

				No. of pits
1 week	RH35 %	Pit depth/μm	40±7	16
		Pit mouth diameter/ μm	82±30	
	RH45 %	Pit depth/μm	28±5	4
		Pit mouth diameter/ μm	32±5	

Regarding pits at higher RH condition 56%, however, no obvious pit was seen as presented in Table 2. The reason probably is that the DSS alloy has a high corrosion resistance compared to other stainless steels, and the amount of Cl<sup>-</sup> within a droplet at this RH may have a strong impact on the pit initiation, this was seen in a study investigated by Timothy et al (Weirich *et al.*, 2019) Who found that for atmospheric initiation the pits of austenite SS depend vastly on the Cl<sup>-</sup> value which was double at lower RH and detected many pits and vice versa at higher RH. In addition, it was investigated that the critical RH for pit to passivate is ranged from 56%-75%, a work achieved on ASS by Van Nam et al (Van Nam, Tada and Nishikata, 2015).

#### 4. CONCLUSION

The effect of both microstructure and variation in relative humidity on atmospheric corrosion pits of 2205 DSS beneath droplets of MgCl<sub>2</sub> was examined.

- The top surface pits appeared mostly layered attack, while the LS and ST planes observed elongated strings
- Mixed oxide inclusions which were mostly Al-Mg-O with inclusions of MnS were revealed on the LS plane of DSS 2205 which was detected by both EDX and XRD analyses.
- The pit was found to be influenced by RH alteration, at RH 35% the trend of pits in 1-week exposure revealed a larger diameter of pit mouth than in RH 45% for the same trend and in both cases, the diameter seemed to be greater at the droplet center than in the edge of the droplet.
- No pit observed at the condition of RH 56%, because it was suggested that elevated [Cl<sup>-</sup>] at low RH might promote more sites of pit initiation and damage than does the lower [Cl<sup>-</sup>] value at higher RH.

#### REFERENCES

- ASTM, E. (1985) (1985) 'Standard practice for maintaining constant relative humidity by means of aqueous solutions', pp. 790–795.
- Cvijović, Z. and Radenković, G. (2006) 'Microstructure and pitting corrosion resistance of annealed duplex stainless steel', *Corrosion Science*, 48(12), pp. 3887–3906. doi: 10.1016/j.corsci.2006.04.003.
- Deng, B. *et al.* (2009) 'Evaluation of localized corrosion in duplex stainless steel aged at 850 °C with critical pitting temperature measurement', *Electrochimica Acta*, 54(10), pp. 2790–2794. doi: 10.1016/j.electacta.2008.11.038.
- Devaraj, A. (2022) 'Directly Monitoring the Shift in Corrosion Mechanisms of a Model FeCrNi Alloy Driven by Electrical Potential', pp. 1–16.
- Ghahari, M. *et al.* (2015) 'Synchrotron X-ray radiography studies of pitting corrosion of stainless steel: Extraction of pit propagation parameters', *Corrosion Science*, 100, pp. 23–35. doi: 10.1016/j.corsci.2015.06.023.
- Haval Bashar MohammedAli (2016) *Atmospheric Pitting Corrosion of Stainless Steel*. University of Birmingham.
- Laya-Guo (2019) 'The effect of relative humidity change on atmospheric pitting corrosion of stainless steel 304L', *Corrosion Science*, 150, pp. doi: 10.1016/j.corsci.2019.01.033.
- Lei, Z. *et al.* (2021) 'Effect of microstructure distribution on pitting initiation and propagation of 2002 duplex stainless steel', *Journal of the Chinese Society of Corrosion and Protection*, 41(6), pp. 837–842. doi: 10.11902/1005.4537.2020.183.
- Li, J. *et al.* (2022) 'Study on Pitting Corrosion Behavior and Semi in-situ Pitting Corrosion Growth Model of 304L SS With Elastic Stress in NaCl Corrosion Environment', *Corrosion Science*, p. 110862.
- Lo, I. H. and Tsai, W. T. (2007) 'Effect of selective dissolution on fatigue crack initiation in 2205 duplex stainless steel', *Corrosion Science*, 49(4), pp. 1847–1861. doi: 10.1016/j.corsci.2006.10.013.
- Maier, B. and Frankel, G. S. (2010) 'Pitting Corrosion of Bare Stainless Steel 304 under Chloride Solution Droplets', *Journal of The Electrochemical Society*, 157(10), p. C302. doi: 10.1149/1.3467850.
- Mampuya, M. B. *et al.* (2021) 'Effect of heat treatment on the microstructure of duplex stainless steel 2205', *Materials Today: Proceedings*, 38(xxxx), pp. 1107–1112. doi: 10.1016/j.matpr.2020.06.196.
- Mohammad-Ali (2016) *Atmospheric Pitting corrosion of Stainless steel*. University of Birmingham.
- Mohammad-Ali (2018) 'The effect of microstructure on the morphology of atmospheric corrosion pits of type 304L', *Corrosion*. doi: 10.5006/2935.
- Moreira, É. P. *et al.* (2023) 'Risk Analysis Related to the Corrosion of Atmospheric Storage Tanks: A Multimethodological Approach Using the FRAM and the ELECTRE-MOr Methods', in *Pervasive Computing and Social Networking*. Springer, pp. 245–257.
- Van Nam, T., Tada, E. and Nishikata, A. (2015) 'Pit initiation and repassivation of stainless steels exposed to cyclic relative humidity changes', *Journal of the Electrochemical Society*, 162(9), p. C419.
- Örnek, C. (2015) 'Performance Characterisation of Duplex Stainless Steel in Nuclear Waste Storage Environment', *Thesis*, pp. 95–110.
- Örnek, C. and Engelberg, D. L. (2015) 'SKPFM measured Volta potential correlated with strain localisation in microstructure to understand corrosion susceptibility of cold-rolled grade 2205 duplex stainless steel', *Corrosion Science*, 99, pp. 164–171. doi: 10.1016/j.corsci.2015.06.035.
- Park, J. H. and Kang, Y. (2017) 'Inclusions in Stainless Steels – A Review', *Steel Research International*, 88(12), pp. 1–26. doi: 10.1002/srin.201700130.
- Potgieter, J. H. *et al.* (1996) 'Corrosion behaviour of duplex stainless steels containing minor ruthenium additions in reducing acid media', *Journal of Applied Electrochemistry*, 26(11), pp. 1103–1110. doi: 10.1007/BF00243734.
- Potgieter, J. H. *et al.* (2008) 'Influence of nickel additions on the corrosion behaviour of low nitrogen 22% Cr series duplex stainless steels', *Corrosion Science*, 50(9), pp. 2572–2579. doi: 10.1016/j.corsci.2008.05.023.
- Pramanik, S., Bera, S. and Ghosh, S. K. (2014) 'Influence of cold rolling on microstructural evolution in 2205 duplex stainless steel', *Steel Research International*, 85(5), pp. 776–783. doi: 10.1002/srin.201300293.
- Rodrigues, D. G. *et al.* (2019) 'Effect of low cold-rolling strain on microstructure, texture, phase transformation, and mechanical properties of 2304 lean duplex stainless steel', *Materials Characterization*, 150(February), pp. 138–149. doi: 10.1016/j.matchar.2019.02.011.
- Sheik, S. *et al.* (2022) 'Effect of microstructural morphology on corrosion susceptibility of austenitic and super austenitic stainless steels', *Materials Today: Proceedings*, 66, pp. 514–518.
- Stewart, J. and Williams, D. E. (1992) 'The initiation of pitting corrosion on austenitic stainless steel: on the role and importance of sulphide inclusions', *Corrosion Science*, 33(3). doi: 10.1016/0010-938X(92)90074-D.
- Street, S. R. *et al.* (2015) 'Atmospheric pitting corrosion of 304L stainless steel: The role of highly concentrated chloride solutions', *Faraday Discussions*, 180, pp. 251–265. doi: 10.1039/c4fd00246f.
- Street, S. R. *et al.* (2018) 'The effect of deposition conditions on atmospheric pitting corrosion location under Evans

- droplets on type 304L stainless steel', *Corrosion*, 74(5), pp. 520–529. doi: 10.5006/2614.
- Tan, H. *et al.* (2011) 'Annealing temperature effect on the pitting corrosion resistance of plasma arc welded joints of duplex stainless steel UNS S32304 in 1.0M NaCl', *Corrosion Science*, 53(6), pp. 2191–2200. doi: 10.1016/j.corsci.2011.02.041.
- Tsutsumi, Y., Nishikata, A. and Tsuru, T. (2005) 'Initial Stage of Pitting Corrosion of Type 304 Stainless Steel under Thin Electrolyte Layers Containing Chloride Ions', *Journal of The Electrochemical Society*, 152(9), p. B358. doi: 10.1149/1.1992470.
- Tsutsumi, Y., Nishikata, A. and Tsuru, T. (2007) 'Pitting corrosion mechanism of Type 304 stainless steel under a droplet of chloride solutions', *Corrosion Science*, 49(3), pp. 1394–1407. doi: 10.1016/j.corsci.2006.08.016.
- Wang, H. and Wang, T. (2021) 'Influence of Hot Rolling and Solution Treatment on the Microstructure and Mechanical Properties of High-Boron Duplex Stainless Steel 0Cr21Ni5Ti-2B', *Metal Science and Heat Treatment*, 63(3–4), pp. 126–131. doi: 10.1007/s11041-021-00658-w.
- Weirich, T. D. *et al.* (2019) 'Humidity Effects on Pitting of Ground Stainless Steel Exposed to Sea Salt Particles', *Journal of The Electrochemical Society*, 166(11), pp. C3477–C3487. doi: 10.1149/2.0551911jes.
- Wranglen, G. (1974) 'Pitting and sulphide inclusions in steel', *Corrosion Science*, 14(5), pp. 331–349. doi: 10.1016/S0010-938X(74)80047-8.
- Yoon, B. J. and Ahn, Y. S. (2022) 'Correction to: Effect of Aging on Pitting Corrosion Resistance of 21Cr Lean Duplex Stainless Steel with Different Molybdenum Contents (Journal of Materials Engineering and Performance, (2022), 10.1007/s11665-022-07478-w)', *Journal of Materials Engineering and Performance*, p. 11665. doi: 10.1007/s11665-022-07588-5.
- Zhang, Y. *et al.* (2020) 'Investigation of micro-electrochemical activities of oxide inclusions and microphases in duplex stainless steel and the implication on pitting corrosion', *Materials and Corrosion*, 71(6), pp. 876–886. doi: 10.1002/maco.201911335.
- Zhu, Y. *et al.* (2020) 'Quantification of the Atmospheric Corrosion of 304 and 2205 Stainless Steels Using Electrochemical Probes Based on Thevenin Electrochemical Equivalent Circuit Model', *Transactions of Tianjin University*, 26(3), pp. 218–227. doi: 10.1007/s12209-020-00242-y.